

NeISF++: Neural Incident Stokes Field for Polarized Inverse Rendering of Conductors and Dielectrics

Chenhao Li^{1,3}, Taishi Ono², Takeshi Uemori¹, Sho Nitta¹,
Hajime Mihara¹, Alexander Gatto², Hajime Nagahara³, Yusuke Moriuchi¹

Sony Semiconductor Solutions Corporation¹, Sony Europe B.V.², Osaka University³

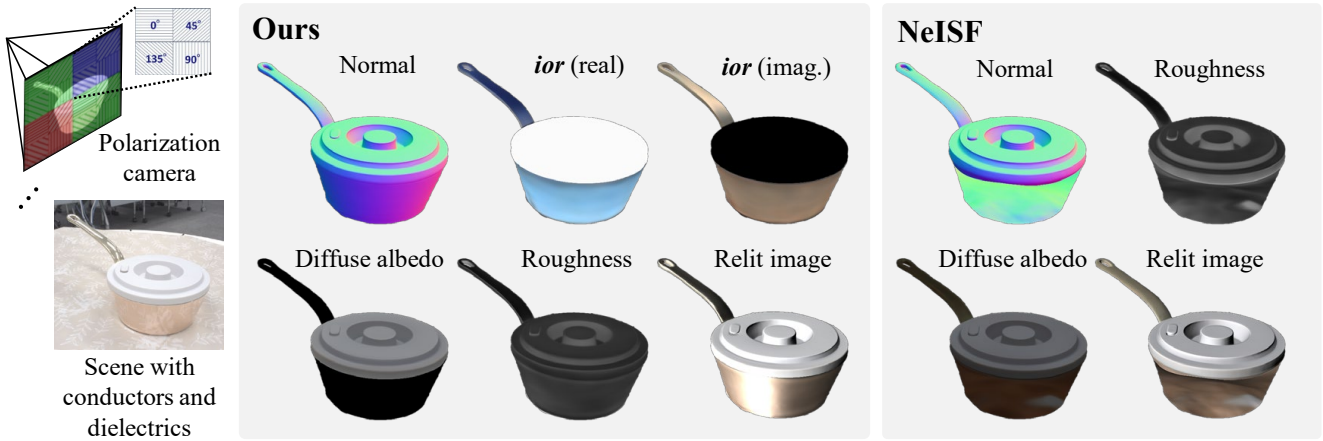


Figure 1. Comparison of the polarized inverse rendering methods. Since NeISF [33] does not model conductors correctly, its geometry and material reconstruction is poor. Our method estimates the complex refractive index of conductors and re-renders the image via a physically-based pBRDF. Therefore, the reconstructed material and geometry are accurate, and the relighting result is glossy. We normalize the real and imaginary parts of the complex refractive index ior , and visualize them separately.

Abstract

Recent inverse rendering methods have greatly improved shape, material, and illumination reconstruction by utilizing polarization cues. However, existing methods only support dielectrics, ignoring conductors that are found everywhere in life. Since conductors and dielectrics have different reflection properties, using previous conductor methods will lead to obvious errors. In addition, conductors are glossy, which may cause strong specular reflection and is hard to reconstruct. To solve the above issues, we propose NeISF++, an inverse rendering pipeline that supports conductors and dielectrics. The key ingredient for our proposal is a general pBRDF that describes both conductors and dielectrics. As for the strong specular reflection problem, we propose a novel geometry initialization method using DoLP images. This physical cue is invariant to intensities and thus robust to strong specular reflections. Experimental results on our synthetic and real datasets show that our method surpasses the existing polarized inverse rendering methods

for geometry and material decomposition as well as downstream tasks like relighting.

1. Introduction

Inverse rendering is a fundamental task in computer vision and computer graphics, which aims to decompose the target scene into 3D properties like geometry, material, and lighting. It is crucial for applications like virtual reality, material science, and game design. The recent progress of inverse rendering has been dominated by neural representations [38], which utilize multilayer perceptrons (MLPs) to efficiently represent geometry [51, 56], material [6], and lighting [54], and greatly improve the reconstruction accuracy. However, the inherent challenge in inverse rendering, the ambiguity problem, still exists. Recovering 3D properties from 2D images is essentially an ill-posed problem, as different combinations of geometry, material, and lighting may result in the same appearance.

An active research field for reducing ambiguity is ap-

plying neural representations beyond conventional cameras. Advanced sensors such as event [44, 45], infrared [58], hyper-spectral [43], fisheye [35], and time-of-flight cameras [2] have been extensively explored. One sophisticated sensor worth mentioning is the polarization camera, which can capture the oscillation direction of light in addition to intensity and color. When the light interacts with the object’s surface, the polarization changes according to the geometry and material. In other words, the captured polarization image contains rich information about geometry and material, thus disambiguating the inverse rendering. To our knowledge, PANDORA [14] is the first work that successfully combines polarization cues and neural representations for an inverse rendering problem. Since then, many follow-up polarized inverse rendering works have been proposed to improve it by supervising with tangent space consistency [10, 20], specifically designed polarimetric loss [11], or considering indirect illumination [33]. However, the same problem with the above polarized inverse rendering works is that they only support dielectric materials. Although dielectrics like rubber, wood, and plastic are common materials, conductors like steel, gold, and aluminum are also unignorable. Applying dielectrics-based inverse rendering methods to conductors causes significant errors. The error mainly comes from two aspects. The first one is dielectrics and conductors have different polarimetric properties, they thus require different material models. The second one is conductors are usually glossy and have strong specular reflections, which increases the ambiguity and requires special treatment.

To solve these issues, we propose NeISF++, a polarized inverse rendering method that supports both conductors and dielectrics. Our framework mainly follows NeISF [33]. Given multi-view polarized images, we represent the geometry as a signed distance field (SDF), the material as a Bidirectional Reflectance Distribution Function (BRDF) field, and the multi-bounced polarized light as an incident Stokes field. Then, a physically-based polarimetric renderer calculates the final outgoing polarized light, and the model is self-supervised. This work focuses on solving the briefly mentioned two error sources: the material model and the strong specular reflection. For the first error source (material model), we propose a general polarimetric BRDF (pBRDF) that describes both conductors and dielectrics. Existing polarized inverse rendering works [14, 33] use Baek pBRDF [4] as the material model, which is specially designed for dielectrics. It describes the captured polarization signal as the combination of diffuse and specular polarization. The diffuse polarization comes from multi-bounced subsurface scattering, and the specular polarization comes from single-bounced mirror reflection. Extending Baek pBRDF to support conductors faces many challenges. For example, visible light can not penetrate the

surface of conductors [13]. Therefore, the diffuse polarization does not exist for conductors. To solve this discrepancy, we propose using a binary indicator to control the existence of the diffuse polarization term. In addition, even for the single-bounced mirror reflection, the properties of conductors and dielectrics are still different. Because the refractive index of dielectrics is a real number, while the refractive index for conductors is a complex number, we implement a general Fresnel reflection term that supports both real and complex numbers to address this problem. For the second error source (strong specular reflection), we propose using the degree of linear polarization (DoLP) images to initialize the SDF. Training the SDF from the initialization of volume rendering works like VolSDF [55] is a common technique used in the existing inverse rendering works [33, 59]. However, poor geometry initialization can damage the final reconstruction results, and the initialization quality is usually low when strong specular reflection exists. An advantage of using polarized images is that we can utilize physical properties such as DoLP, which is independent of the light intensity and strongly related to the geometry. With these advantages, we argue that DoLP is a better image domain for geometry initialization than intensity images. By solving the two error sources, NeISF++ significantly improves geometry and material reconstruction when both conductors and dielectrics exist. Additionally, because of the correct modeling of conductors, the relighting results are much more realistic than the previous work [33] (Fig. 1). To summarize, our contributions can be seen as proposing:

- NeISF++, the first polarized inverse rendering pipeline with pBRDF supporting conductors and dielectrics.
- A novel geometry initialization approach using DoLP images, which is robust to strong specular reflections.
- A real and synthetic multi-view polarimetric dataset consists of objects containing conductors and dielectrics.

The code and dataset will be made public upon acceptance.

2. Related Works

2.1. Scene representations

Exploring appropriate 3D representations is a crucial task for inverse rendering. Conventional renderers usually represent geometry as meshes and material as BRDFs and render the image via path tracing. However, these representations do not always work well for inverse rendering. For example, meshes are discrete data structures; the differentiability must be considered during the optimization. BRDF parameters are usually given by texture maps, which have resolution and sampling issues. Although path tracing creates photorealistic images, the computational cost is large. On the other hand, recent neural rendering works [38] show the possibility of representing 3D scenes using neural networks, which are compact and efficient. We mainly cover

the three important aspects of inverse rendering, which are geometry, material, and lighting, and describe how to represent them using neural networks.

Geometry The original NeRF [38] represents geometry as a density field. Although it shows stunning results in novel-view synthesis, the reconstructed geometry is noisy. On the other hand, some works like IDR [57] use SDF to represent the geometry and show a smooth surface estimation. Later works like VolSDF [55], NeuS [51], or Objects as volumes [39] take advantage of both worlds by building connections between SDF and density via Laplace, logistic, or Gaussian functions. Another research branch is representing geometries as 3D [28] or 2D [22] Gaussians. Although these methods greatly accelerate the training and inference time, the reconstruction quality of geometry is still controversial [22] compared to SDF-based methods. Therefore, we use VolSDF [55] as our geometry representation.

Material Parametric BRDFs, which represent BRDF as a parametric model, are a commonly used method in conventional renderers. The parameters are usually provided via 2D texture maps, and UV mapping functions are used to project 2D points to 3D spaces. However, texture maps are discrete data, which may cause aliasing problems and thus require advanced sampling techniques. Recently, several neural rendering works [6] have shown that the texture can be represented as a continuous 3D function using MLPs. Given the 3D position of the object’s surface, the MLP directly returns the BRDF parameters without sampling. As for the selection of BRDF models, most existing neural rendering works [12, 21, 26, 40, 52, 54, 59, 62] use Disney BRDF [8]. However, this BRDF only describes the material property regarding light intensity. To describe the material property of polarization, pBRDFs [4, 23, 24, 30] are desired. Among them, Baek pBRDF [4] is commonly used in polarized inverse rendering works. However, one limitation is that it only supports dielectric objects, which is problematic because conductors are also our target objects. We extend this pBRDF to also support conducts.

Lighting Another important part of inverse rendering is the lighting representation. Early works only model the single-bounced light as a spherical Gaussian [6, 60], low-resolution environment map [21, 61], or split-sum approximation [7, 40]. However, a strong limitation of only modeling the single-bounced is that their models can not handle phenomenons such as inter-reflection. Multi-bounce simulation is expensive and prone to noise when using the traditional Monte Carlo-based path tracing. Various solutions have been proposed, such as separating the direct and indirect light using a visibility mask [26, 62] or a bounding sphere [36], and modeling them individually, pre-computing the multi-bounced light [53], only computing the last bounce explicitly, and using MLPs to record the rest bounces implicitly [19, 54, 59]. NeISF [33] is the

first work that considers the multi-bounced polarized light by proposing the incident Stokes field. We follow this light representation.

2.2. Polarization in inverse rendering

Many works use polarization cues to disambiguate inverse rendering since polarization cues are sensitive to geometry and material. Single-view methods are mainly based on deep neural networks, and they have shown some progress in the inverse rendering of opaque [15, 16], transparent [46], or translucent [32] objects. However, the disadvantage of using data-driven methods is the lack of data for real-world objects. Using synthetic data to train the network may solve the problem of insufficient data, but it also introduces additional problems like domain gaps. Multi-view methods [3, 63] are mainly based on analysis-by-synthesis, and the performance bottleneck comes from the aforementioned scene representation problem. Many works have recently attempted to combine neural representation and polarization cues. Early works mainly focus on the novel-view synthesis of polarimetric fields [42] or Spectro-polarimetric fields [29]. Lately, PANDORA [14] has been proposed for geometry reconstruction, and follow-up works have improved it by introducing tangent space consistency (MVAS [10], NeRSP [20]) or polarimetric losses (PISR [11]). NeISF [33] is the first neural rendering work that supports pBRDF decomposition, and it is the most similar work to ours. However, the strong limitation is that it only supports dielectrics. Our work can be considered a general version supporting conductors and dielectrics.

2.3. Inverse rendering of specular objects

The original NeRF [38] tends to create fake specular reflections by foggy effects. To solve the problem, ideas such as modeling a 3D varying refractive index [5] and directional encoding [37, 48] have been proposed. Later, some works attempt to reconstruct the accurate geometry of glossy objects by computing a reflection score map via an abnormal detector [17] or the difference between the albedo and intensity [50]. Recently, several inverse rendering works also put their focus on reflective objects by considering the multi-bounce reflection [36], integrating material priors [31], and using a novel parallax-aware non-distant lighting representation [9]. We show that the DoLP image is a powerful cue for the geometry initialization of glossy objects because the DoLP is invariant to light intensities and thus robust to the strong specular reflection.

3. Preliminary

We briefly introduce the mathematical representation of polarized light and material and recap NeISF [33].

3.1. Background of Polarization

Stokes vectors and Mueller matrices are the mathematical descriptions of the polarized light and optical elements. When only linear polarization is considered, Stokes vectors $\mathbf{s} \in \mathbb{R}^3$ have three elements $[s_0, s_1, s_2]$, where s_0 is the unpolarized light intensity, s_1 is the 0° over 90° linear polarization, and s_2 is the 45° over 135° linear polarization. Mueller matrices $\mathbf{M} \in \mathbb{R}^{3 \times 3}$ describe the polarimetric property of the material and are used to multiply Stokes vectors to represent the polarimetric light-object interaction.

Baek pBRDF [4] is commonly used in the recent polarized inverse rendering works [14, 33]. It separates the material model into diffuse and specular polarization. Diffuse polarization \mathbf{M}_{dif} describes the process of light passing through the surface, undergoing multiple scattering events inside the object, leaving the object, and being captured by the sensor:

$$\mathbf{M}_{\text{dif}} = \left(\frac{a}{\pi} \cos \theta_i\right) \mathbf{F}_o^T \cdot \mathbf{D} \cdot \mathbf{F}_i^T, \quad (1)$$

where a is the diffuse albedo, $\theta_{i,o}$ denotes the incident / outgoing angle, $\mathbf{D} \in \mathbb{R}^{3 \times 3}$ is a depolarizer, and $\mathbf{F}_{i,o}^T \in \mathbb{R}^{3 \times 3}$ is the Fresnel transmission term. Specular polarization \mathbf{M}_{spec} comes from the single-bounced mirror reflection:

$$\mathbf{M}_{\text{spec}} = k_s \frac{DG}{4 \cos \theta_o} \mathbf{F}^R, \quad (2)$$

where k_s is the specular coefficient, D is the GGX distribution function [49], G is the Smith function, and $\mathbf{F}^R \in \mathbb{R}^{3 \times 3}$ is the Fresnel reflection term.

3.2. Recap of NeISF

Polarimetric rendering equation NeISF [33] uses Baek pBRDF as the material model. As a result, the corresponding Rendering Equation [27] is:

$$\mathbf{s} = \int_{\Omega} \mathbf{R}_{\text{dif}}^{\text{cam}} \cdot \mathbf{M}_{\text{dif}} \cdot \mathbf{s}_{\text{dif}}^r + \mathbf{R}_{\text{spec}}^{\text{cam}} \cdot \mathbf{M}_{\text{spec}} \cdot \mathbf{s}_{\text{spec}}^r d\omega_i, \quad (3)$$

where \mathbf{s} is the final Stokes vector captured by the sensor, \mathbf{R}^{cam} is the rotation Mueller matrix which rotates the outgoing Stokes vector to the camera’s reference frame, \mathbf{s}^r is the incident Stokes vector which is already rotated to the reference frame of the material Mueller matrix \mathbf{M} , ω_i is the incident direction, and the subscript dif/spec denotes the diffuse/specular term. The integral of Eq. 3 is solved by a Fibonacci sphere sampling.

Neural fields They represent the geometry as an SDF $\mathbb{S} : \mathbf{x} \rightarrow d$, where \mathbf{x} is the 3D position, d is the distance, and the normal \mathbf{n} is obtained by computing the gradient of the SDF. The material is represented as a BRDF field $\mathbb{B} : \mathbf{x} \rightarrow \{r, \mathbf{a}\}$, where r is the roughness and \mathbf{a} is the diffuse albedo. The lighting is represented as an incident Stokes field $\mathbb{L} : \{\mathbf{x}, \omega_i\} \rightarrow \{\mathbf{s}_{\text{dif}}^r, \mathbf{s}_{\text{spec}}^r\}$. Then Eq. 3 is used for rendering the Stokes vector \mathbf{s} , and the entire model training is self-supervised by the GT Stokes vectors.

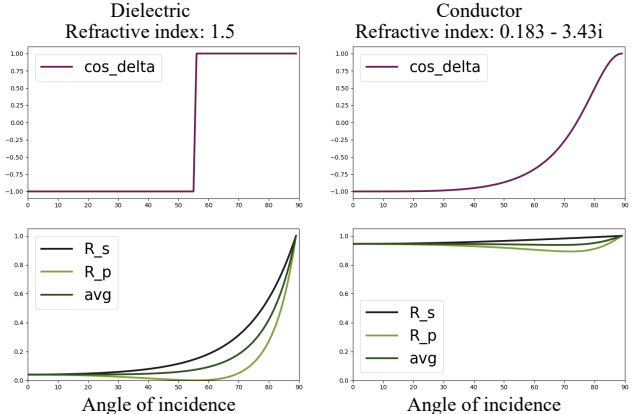


Figure 2. Cosine values of phase delay (upper) and reflection coefficients (bottom) of a typical conductor (gold at 633nm) and dielectric (refractive index equals 1.5). “R_s” and “R_p” are the perpendicular and parallel components of reflectance, “avg” denotes their average value.

4. NeISF++

Given multi-view polarized images of objects containing dielectrics and conductors, we reconstruct geometry and material simultaneously. The reconstructed 3D assets are compatible with conventional renderers that are capable of downstream tasks such as relighting and material editing. The sections are arranged as follows: We introduce the material model that is designed for both conductors and dielectrics in Sec. 4.1. The training is divided into two stages: the first stage is the geometry initialization using DoLP images (Sec. 4.2), and the second stage is the joint optimization (Sec. 4.3) of geometry, material, and lighting using the proposed material model.

4.1. Material model

As briefly mentioned before, the previous polarized inverse rendering works [14, 33] use Baek pBRDF as their material model, which only supports dielectrics. Extending this pBRDF also to support conductors requires solving some discrepancies. Because conductors are practically opaque, [13], subsurface scattering, which is the key factor creating diffuse polarization, does not exist for conductors. We propose a simple yet efficient solution by adding a binary indicator m before the diffuse polarization term. As a result, Eq. 3 should be rewritten as:

$$\mathbf{s} = \int_{\Omega} m \mathbf{R}_{\text{dif}}^{\text{cam}} \cdot \mathbf{M}_{\text{dif}} \cdot \mathbf{s}_{\text{dif}}^r + \mathbf{R}_{\text{spec}}^{\text{cam}} \cdot \mathbf{M}_{\text{spec}} \cdot \mathbf{s}_{\text{spec}}^r d\omega_i. \quad (4)$$

The value of m is either set to 0 for conductors or 1 for dielectrics. Note that, unlike the metallic term used in Disney BRDF [8] is a continuous parameter, for physical realism, m should be a discrete parameter. Even if the existence of

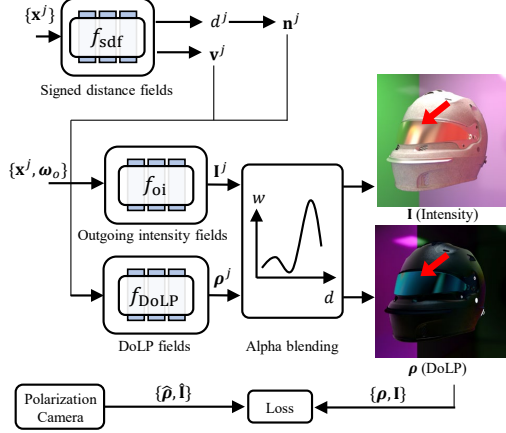


Figure 3. Geometry initialization pipeline using both intensity and DoLP images. Intensity on the conductor area suffers from strong specular reflections, while DoLP images are less affected by strong specular reflections. The initialized signed distance fields f_{sdf} will continue to be trained in the joint optimization stage.

the diffuse polarization problem has been solved by the binary indicator, the specular polarization term is still different for conductors and dielectrics. Concretely, the refractive index for dielectrics is real numbers, and the refractive index for conductors is complex numbers. This causes the reflection coefficients and the phase delay of the Fresnel reflection term \mathbf{F}^R to be dramatically different for conductors and dielectrics (See Fig. 2 for reference). Unfortunately, \mathbf{F}^R in Baek pBRDF does not support complex numbers:

$$\mathbf{F}^R = \begin{bmatrix} R^+ & R^- & 0 \\ R^- & R^+ & 0 \\ 0 & 0 & R^\times \cos \Delta \end{bmatrix}, \quad (5)$$

because the calculation of reflection coefficients R^+ , R^- is designed for real numbers, and the phase delay Δ is hard coded to π or 0 when the incident angle is less or larger than the Brewster angle. We calculate the reflection coefficients and phase delay based on the Fresnel wave theory [13], so the Fresnel reflection term supports a complex refractive index (Details can be found in the supplementary document). **Assumptions** Theoretically, the binary indicator m can be optimized jointly just like the other pBRDF parameters. However, adding parameters to be optimized significantly increases the ambiguity problem. Therefore, we assume m is given by the user-specified conductor-dielectric mask during the training to reduce the difficulty of the task. In addition, we only estimate the refractive index for the conductor part, and for the dielectric part, we follow NeISF [33] to assume it as 1.5.

4.2. Geometry initialization

In this section, we demonstrate that DoLP is a suitable image space for geometry initialization, especially when

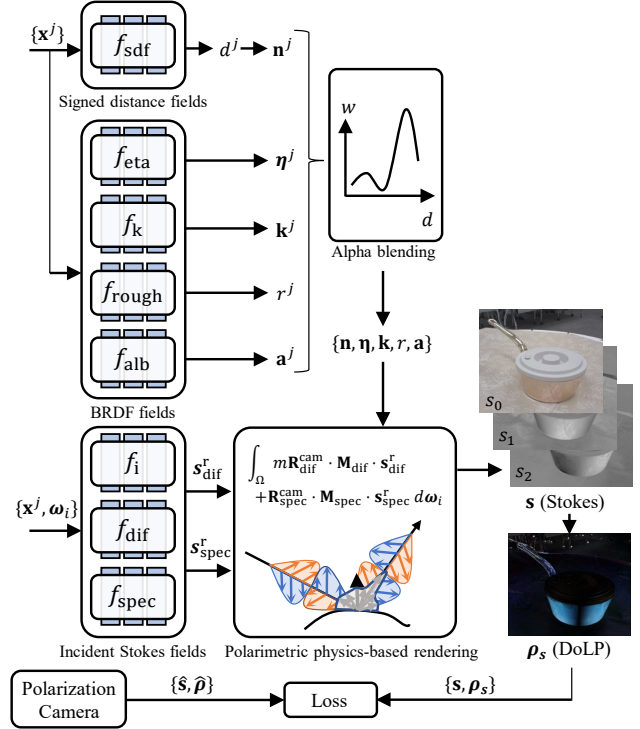


Figure 4. Overview of the joint optimization stage.

strong specular reflections exist. To stabilize the training, previous inverse rendering works [59] usually start the training with geometry initialized by volume rendering techniques [55]. However, a well-known problem with these methods is their bad performance for reflective objects. The challenging part of reflective objects is their view-dependent appearance property. Although these techniques have already modeled the view-dependent appearance property by inputting the view direction to MLPs, the inherent ambiguity of inverse rendering usually leads to wrong geometry reconstruction. This wrong geometry reconstruction behavior will be escalated by specular reflections with strong intensities. For example, the reflected light directly comes from the light source, which is commonly observed daily. We propose using DoLP to train a VoISDF [55] to initialize the geometry:

$$f_{\text{DoLP}}(\mathbf{x}^j, \boldsymbol{\omega}_o, \mathbf{n}^j, \mathbf{v}^j) = \boldsymbol{\rho}^j, \quad (6)$$

where f_{DoLP} is an MLP, \mathbf{x}^j , \mathbf{n}^j , \mathbf{v}^j , $\boldsymbol{\rho}^j$ are the position, normal, feature vector, and DoLP at the sampled point along the ray. $\boldsymbol{\omega}_o$ is the outgoing direction. The normal and feature vectors are given by the SDF net f_{sdf} . The DoLP of the object surface is computed via alpha-blending $\boldsymbol{\rho} = \sum_{j=1}^N w^j \boldsymbol{\rho}^j$, and w^j is the weight calculated by the volume rendering. The loss is computed by the L_1 loss between the GT DoLP and the estimated one. The aforementioned strong specular reflection intensity problem does not exist in

DoLP images because it is invariant to light intensity (See Fig. 3 for reference). Besides, DoLP is strongly related to geometry, making it suitable for geometry initialization. To stabilize the training, we still use the intensity images to compute the loss, just like VolSDF [55]. However, we only assign the intensity loss a tiny weight. As a result, the loss function is:

$$L_{\text{init}} = \lambda_{\rho} L_1(\rho, \hat{\rho}) + \lambda_{\mathbf{I}} L_1(\mathbf{I}, \hat{\mathbf{I}}) + \lambda_{\text{Eik}} L_{\text{Eik}}, \quad (7)$$

where $\hat{\mathbf{I}}, \hat{\rho}$ are the GT intensity and DoLP images, \mathbf{I}, ρ are the reconstructed intensity and DoLP images. L_{Eik} is the Eikonal regularization [18] to avoid the everywhere zero solution of the SDF net.

4.3. Joint optimization

After the geometry initialization in Sec. 4.2, we jointly optimize the geometry, material, and lighting (Fig. 4). Because the overall structure follows NeISF [33], we only focus on the key contribution of this work, and the entire model description can be found in the supplementary material. We represent geometry as an SDF, material as a BRDF field, and lighting as an incident Stokes field. The main difference comes from the BRDF field. Unlike common dielectrics such as acrylic glass (1.49), polypropylene plastic (1.49), and quartz (1.458), have similar refractive index ior , the ior of conductors varying significantly among common conductors such as aluminum, copper, steel. In addition, the ior of conductors are spectrally varying, affecting the object’s appearance a lot. Therefore, it is impossible to assume the ior as a constant for conductors. To solve this problem, we estimate the ior in the BRDF field as well. The ior of conductors is a complex number, and it can be represented as follows: $ior = \eta - ki$, where $\eta \in \mathbb{R}^3$ is the real part and $k \in \mathbb{R}^3$ is the imaginary part. Therefore the BRDF field should be rewritten as: $\mathbb{B} : \mathbf{x} \rightarrow \{r, \mathbf{a}, \eta, \mathbf{k}\}$. After estimating η and k , we combine and convert them to complex numbers. As for the dielectric part, NeISF [33] shows an impressive result even with ior assumed as a constant. Following their work, we also assume the ior of dielectrics as 1.5. After estimating all parameters, the final Stokes vectors are rendered by Eq. 4. Note that the rendering equation should be repeated three times for rendering RGB channels. We compute L_1 loss between the reconstructed Stokes vectors and the GT. In addition, we also reconstruct the DoLP image: $\rho_s = \sqrt{\mathbf{s}[1]^2 + \mathbf{s}[2]^2} / \mathbf{s}[0]$, and the loss function is:

$$L_{\text{joint}} = \lambda_{\rho_s} L_1(\rho_s, \hat{\rho}) + \lambda_s L_1(\mathbf{s}, \hat{\mathbf{s}}) + \lambda_{\text{Eik}} L_{\text{Eik}}, \quad (8)$$

where $\mathbf{s}, \hat{\mathbf{s}}$ are the reconstructed and GT Stokes vectors. We utilize the auto-differentiation of complex numbers feature in PyTorch [41] so that the entire pipeline is differentiable.

5. Experiments

5.1. Datasets

Although many polarized multi-view datasets exist, none contain both conductors and dielectrics. In addition, most of the existing datasets are LDR, which may suffer from unknown gamma correction and saturation problems. We propose real and synthetic multi-view polarized HDR datasets containing conductors and dielectrics. For the synthetic dataset, we rendered images using Mitsuba 3 [25]. We rendered 110 views for each scene with GT Stokes vectors, DoLP images, object masks, conductor-dielectric masks, diffuse albedo maps, roughness maps, and refractive index maps. We split the dataset and used 100 views for training and 10 for evaluation. For the real dataset, we captured images with a polarization camera (FLIR BFS-U3-51S5PC-C). Because the camera only supports LDR capture, we captured images with different exposure times and composited them to obtain HDR images. For each scene, we captured roughly 100 views for training and 2-4 for evaluation. For each view, we captured four linearly polarized images, which are used to calculate the Stokes vectors and DoLP images. We also manually created object masks and conductor-dielectric masks using Photoshop [1].

5.2. Baselines

To our knowledge, this is the first work focusing on the polarized inverse rendering of both conductors and dielectrics, so looking for competitors with exactly the same target is difficult. As a result, NeISF [33] is the second best choice. Although it does not support the refractive index estimation of conductors, the geometry, roughness, diffuse albedo, and relighting results can be compared. In addition, although some works [10, 11, 14] do not support material estimation, they still use polarization for geometry reconstruction. We selected the most representative work PANDORA [14] as our competitor. On the other hand, although some works do not use polarization cues, they are specifically designed for specular object reconstruction. Among them, we chose the most influential work NeRO [36] to compare the geometry reconstruction. Finally, we also used a famous volume rendering work VolSDF [55] as the competitor. We also conducted an ablation study. Instead of using the geometry initialization method proposed in Sec. 4.2 (we name it VolSDF-DoLP), we used the original VolSDF [55] to initialize the geometry and train the joint optimization stage. We call this ablated version **Ours-a**.

5.3. Results

Geometry reconstruction We compare surface normal results for synthetic data qualitatively (Fig. 5) and quantitatively (Tab. 1). Due to the lack of GT data for the real data, we only provide qualitative results in Fig. 6.

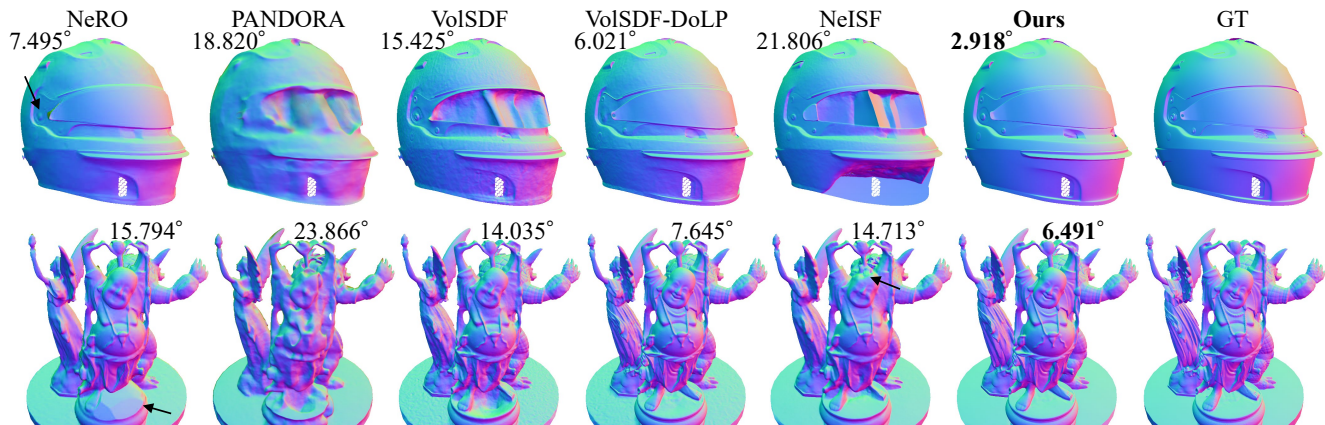


Figure 5. Surface normal results of synthetic data. Mean angular errors are on the top. Our method shows a better reconstruction quality than NeRO [36] and PANDORA [14]. NeISF [33] failed because of the wrong material model and the poor geometry initialization of VolSDF [55]. Our geometry initialization method VolSDF-DoLP shows a better reconstruction quality.

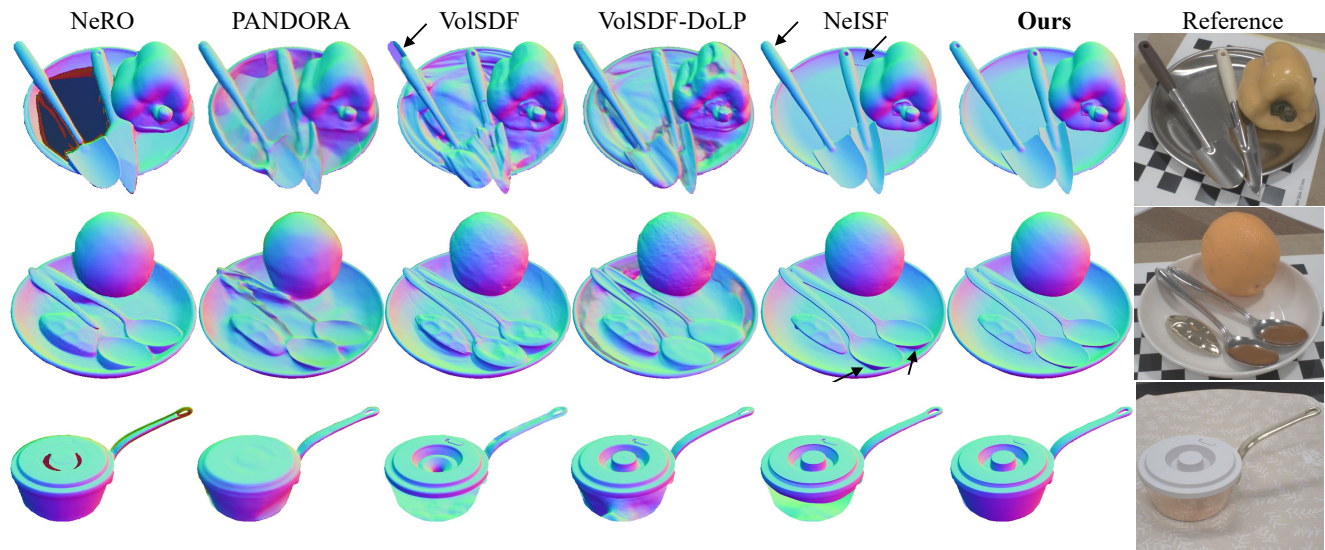


Figure 6. Surface normal reconstruction results of real data.

Material reconstruction We report the qualitative results of material reconstruction in Fig. 8 and quantitative results in Tab. 2. Although NeRO [36] also supports material estimation, the BRDF model differs from ours. Therefore, it is meaningless to compare the reconstructed BRDF parameters. NeISF [33] does not support the complex refractive index reconstruction, thus we only compare the albedo and roughness. In addition, we also compare with “Ours-a”.

Relighting We demonstrate one important downstream task of inverse rendering: relighting. We compare the results between our method and NeISF [33] in Fig. 7.

6. Limitations and Future Works

Conductor-dielectric masks are assumed as known parameters in this work. However, manually creating the masks is time-consuming and labor-intensive, which may limit the method’s practicality. Therefore, the automatic generation of this mask is desired. We discuss two potential solutions to this problem, which are data-driven and error-driven. For the data-driven approach, one can consider mask generation as a material segmentation task [34, 47] through training a neural network on a large labeled dataset. For the error-driven approach, one can optimize a material mask to separate conductors and dielectrics according to the rendering errors, which have been verified effective for separating emitters and non-emitters [53].

	Ours	Ours-a	VolSDF-DoLP	VolSDF [55]	NeISF [33]	PANDORA [14]	NeRO [36]
Stanford scan	6.487°	6.480°	7.641°	11.754°	14.022°	21.740°	13.352°
Helmet	1.789°	2.400°	4.715°	8.829°	10.303°	13.212°	5.001°

Table 1. Surface normal reconstruction results on our synthetic dataset. Mean angular errors are computed on the average of 10 test views.

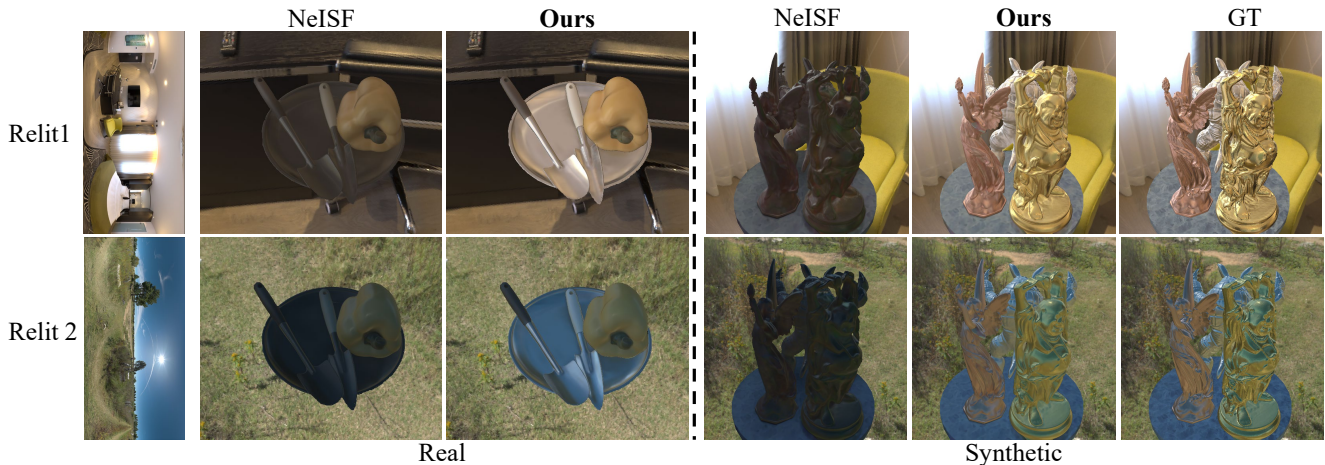


Figure 7. Relighting results. Even though NeISF [33] can reconstruct plausible geometry, the relighting result for the conductor part is not realistic due to the inaccurate material model. While our results are shiny and similar to the GT.

		Ours	Ours-a	NeISF [33]
Stanford scan	Roughness	.0706	.0821	.2425
	Albedo	.0468	.1289	.2954
	Eta	.0685	.0722	-
	K	.4300	.5107	-
Helmet	Roughness	.0161	.0199	.2075
	Albedo	.0615	.0716	.4467
	Eta	.0717	.1937	-
	K	.6526	1.327	-

Table 2. Material reconstruction results on the proposed synthetic dataset. We compute the mean absolute errors on 10 test views for all material parameters. We count the errors of Eta and K for the conductor part and albedo for the dielectric part. Roughness errors are computed over the entire object.

7. Conclusion

We have proposed NeISF++, a polarized inverse rendering pipeline that supports both conductors and dielectrics. It relies on the following novelties. The first one is a general pBRDF, which describes both conductors and dielectrics. The second one is a novel geometry initialization method using DoLP images. With these two novelties, NeISF++ outperforms the existing inverse rendering models for geometry and material decomposition on both the proposed synthetic and real-world datasets. The relighting compari-

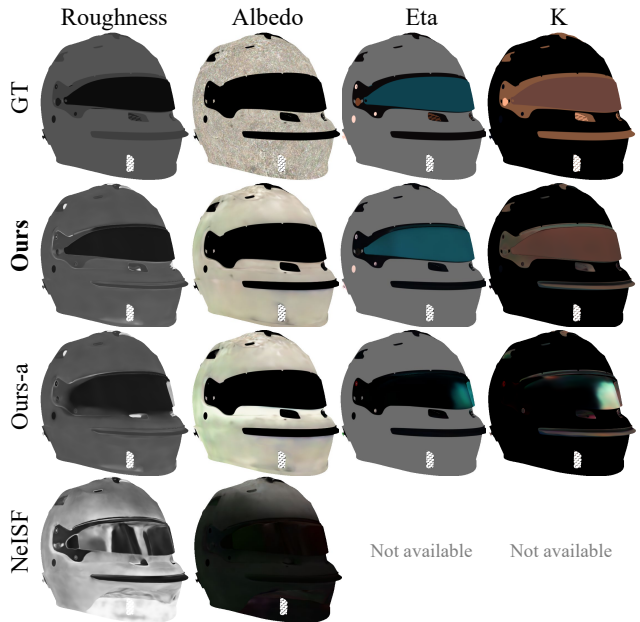


Figure 8. Material reconstruction result. Eta and K are the real and imaginary components of the complex refractive index. We normalize them to 0-1 for visualization. NeISF [33] completely failed to reconstruct the material due to the wrong geometry reconstruction. “Ours” are significantly better than “Ours-a”, especially for the refractive index reconstruction.

son between our method and NeISF [33] also shows the importance of correctly modeling conductors. However, several limitations mentioned in Sec. 6 still exist and are worth further exploration.

References

- [1] Adobe Inc. Adobe photoshop. 6
- [2] Benjamin Attal, Eliot Laidlaw, Aaron Gokaslan, Changil Kim, Christian Richardt, James Tompkin, and Matthew O’Toole. Törf: Time-of-flight radiance fields for dynamic scene view synthesis. *NeurIPS*, 34:26289–26301, 2021. 2
- [3] Dejan Azinović, Olivier Maury, Christophe Hery, Matthias Nießner, and Justus Thies. High-res facial appearance capture from polarized smartphone images. In *CVPR*, pages 16836–16846, 2023. 3
- [4] Seung-Hwan Baek, Daniel S Jeon, Xin Tong, and Min H Kim. Simultaneous acquisition of polarimetric svbrdf and normals. *ACM TOG*, 37(6):268–1, 2018. 2, 3, 4
- [5] Mojtaba Bemana, Karol Myszkowski, Jeppe Revall Frisvad, Hans-Peter Seidel, and Tobias Ritschel. Eikonal fields for refractive novel-view synthesis. In *SIGGRAPH*, pages 1–9, 2022. 3
- [6] Mark Boss, Raphael Braun, Varun Jampani, Jonathan T. Barron, Ce Liu, and Hendrik P.A. Lensch. Nerd: Neural reflectance decomposition from image collections. In *ICCV*, 2021. 1, 3
- [7] Mark Boss, Varun Jampani, Raphael Braun, Ce Liu, Jonathan T. Barron, and Hendrik P.A. Lensch. Neural-pil: Neural pre-integrated lighting for reflectance decomposition. In *NeurIPS*, 2021. 3
- [8] Brent Burley and Walt Disney Animation Studios. Physically-based shading at disney. In *SIGGRAPH*, volume 2012, pages 1–7, 2012. 3, 4
- [9] Guangyan Cai, Fujun Luan, Miloš Hašan, Kai Zhang, Sai Bi, Zexiang Xu, Iliyan Georgiev, and Shuang Zhao. Pbirnie: Glossy object capture under non-distant lighting. *arXiv preprint arXiv:2408.06878*, 2024. 3
- [10] Xu Cao, Hiroaki Santo, Fumio Okura, and Yasuyuki Matsushita. Multi-view azimuth stereo via tangent space consistency. In *CVPR*, pages 825–834, 2023. 2, 3, 6
- [11] Guangcheng Chen, Yicheng He, Li He, and Hong Zhang. Pidr: Polarimetric neural implicit surface reconstruction for textureless and specular objects. *arXiv preprint arXiv:2409.14331*, 2024. 2, 3, 6
- [12] Ziang Cheng, Junxuan Li, and Hongdong Li. Wildlight: In-the-wild inverse rendering with a flashlight. In *CVPR*, pages 4305–4314, 2023. 3
- [13] Edward Collett. Field guide to polarization. Spie Bellingham, 2005. 2, 4, 5
- [14] Akshat Dave, Yongyi Zhao, and Ashok Veeraraghavan. Pandora: Polarization-aided neural decomposition of radiance. In *ECCV*, pages 538–556, 2022. 2, 3, 4, 6, 7, 8
- [15] Valentin Deschaintre, Yiming Lin, and Abhijeet Ghosh. Deep polarization imaging for 3d shape and svbrdf acquisition. In *CVPR*, pages 15567–15576, 2021. 3
- [16] Jin Duan, Youfei Hao, Ju Liu, Cai Cheng, Qiang Fu, and Huilin Jiang. End-to-end neural network for pbrdf estimation of object to reconstruct polarimetric reflectance. *Optics Express*, 31(24):39647–39663, 2023. 3
- [17] Wenhang Ge, Tao Hu, Haoyu Zhao, Shu Liu, and Ying-Cong Chen. Ref-neus: Ambiguity-reduced neural implicit surface learning for multi-view reconstruction with reflection. In *ICCV*, pages 4251–4260, 2023. 3
- [18] Amos Gropp, Lior Yariv, Niv Haim, Matan Atzmon, and Yaron Lipman. Implicit geometric regularization for learning shapes. In *Proceedings of the 37th International Conference on Machine Learning*, pages 3789–3799, 2020. 6
- [19] Saeed Hadadan, Shuhong Chen, and Matthias Zwicker. Neural radiosity. *ACM TOG*, 40(6):1–11, 2021. 3
- [20] Yufei Han, Heng Guo, Koki Fukai, Hiroaki Santo, Boxin Shi, Fumio Okura, Zhanyu Ma, and Yunpeng Jia. Nersp: Neural 3d reconstruction for reflective objects with sparse polarized images. In *CVPR*, pages 11821–11830, 2024. 2, 3
- [21] Jon Hasselgren, Nikolai Hofmann, and Jacob Munkberg. Shape, light, and material decomposition from images using monte carlo rendering and denoising. *NeurIPS*, 35:22856–22869, 2022. 3
- [22] Binbin Huang, Zehao Yu, Anpei Chen, Andreas Geiger, and Shenghua Gao. 2d gaussian splatting for geometrically accurate radiance fields. In *SIGGRAPH*, pages 1–11, 2024. 3
- [23] Inseung Hwang, Daniel S Jeon, Adolfo Munoz, Diego Gutierrez, Xin Tong, and Min H Kim. Sparse ellipsometry: portable acquisition of polarimetric svbrdf and shape with unstructured flash photography. *ACM TOG*, 41(4):1–14, 2022. 3
- [24] Tomoki Ichikawa, Yoshiki Fukao, Shohei Nobuhara, and Ko Nishino. Fresnel microfacet brdf: Unification of polarimetric surface-body reflection. In *CVPR*, pages 16489–16497, 2023. 3
- [25] Wenzel Jakob, Sébastien Speierer, Nicolas Roussel, and Dario Vicini. Dr.jit: A just-in-time compiler for differentiable rendering. *ACM TOG*, 41(4), 2022. 6
- [26] Haian Jin, Isabella Liu, Peijia Xu, Xiaoshuai Zhang, Songfang Han, Sai Bi, Xiaowei Zhou, Zexiang Xu, and Hao Su. Tensor: Tensorial inverse rendering. In *CVPR*, pages 165–174, 2023. 3
- [27] James T Kajiya. The rendering equation. In *Proceedings of the 13th annual conference on Computer graphics and interactive techniques*, pages 143–150, 1986. 4
- [28] Bernhard Kerbl, Georgios Kopanas, Thomas Leimkühler, and George Drettakis. 3d gaussian splatting for real-time radiance field rendering. *ACM TOG*, 42(4):139–1, 2023. 3
- [29] Youngchan Kim, Wonjoon Jin, Sunghyun Cho, and Seung-Hwan Baek. Neural spectro-polarimetric fields. In *SIGGRAPH Asia*, pages 1–11, 2023. 3
- [30] Yuhi Kondo, Taishi Ono, Legong Sun, Yasutaka Hirasawa, and Jun Murayama. Accurate polarimetric brdf for real polarization scene rendering. In *ECCV*, pages 220–236, 2020. 3
- [31] Shuichang Lai, Letian Huang, Jie Guo, Kai Cheng, Bowen Pan, Xiaoxiao Long, Jiangjing Lyu, Chengfei Lv, and Yanwen Guo. Glossygs: Inverse rendering of glossy objects

- with 3d gaussian splatting. *arXiv preprint arXiv:2410.13349*, 2024. 3
- [32] Chenhao Li, Trung Thanh Ngo, and Hajime Nagahara. Deep polarization cues for single-shot shape and subsurface scattering estimation. *arXiv preprint arXiv:2407.08149*, 2024. 3
- [33] Chenhao Li, Taishi Ono, Takeshi Uemori, Hajime Mihara, Alexander Gatto, Hajime Nagahara, and Yusuke Moriuchi. Neisf: Neural incident stokes field for geometry and material estimation. In *CVPR*, pages 21434–21445, 2024. 1, 2, 3, 4, 5, 6, 7, 8, 9
- [34] Yupeng Liang, Ryosuke Wakaki, Shohei Nobuhara, and Ko Nishino. Multimodal material segmentation. In *CVPR*, pages 19800–19808, 2022. 7
- [35] Zimu Liao, Siyan Chen, Rong Fu, Yi Wang, Zhongling Su, Hao Luo, Linning Xu, Bo Dai, Hengjie Li, Zhilin Pei, et al. Fisheye-gs: Lightweight and extensible gaussian splatting module for fisheye cameras. *arXiv preprint arXiv:2409.04751*, 2024. 2
- [36] Yuan Liu, Peng Wang, Cheng Lin, Xiaoxiao Long, Jiepeng Wang, Lingjie Liu, Taku Komura, and Wenping Wang. Nero: Neural geometry and brdf reconstruction of reflective objects from multiview images. *ACM TOG*, 42(4):1–22, 2023. 3, 6, 7, 8
- [37] Li Ma, Vasu Agrawal, Haithem Turki, Changil Kim, Chen Gao, Pedro Sander, Michael Zollhöfer, and Christian Richardt. Specnerf: Gaussian directional encoding for specular reflections. In *CVPR*, pages 21188–21198, 2024. 3
- [38] Ben Mildenhall, Pratul P Srinivasan, Matthew Tancik, Jonathan T Barron, Ravi Ramamoorthi, and Ren Ng. Nerf: Representing scenes as neural radiance fields for view synthesis. In *ECCV*, pages 405–421, 2020. 1, 2, 3
- [39] Bailey Miller, Hanyu Chen, Alice Lai, and Ioannis Gkioulekas. Objects as volumes: A stochastic geometry view of opaque solids. In *CVPR*, pages 87–97, 2024. 3
- [40] Jacob Munkberg, Jon Hasselgren, Tianchang Shen, Jun Gao, Wenzheng Chen, Alex Evans, Thomas Müller, and Sanja Fidler. Extracting triangular 3d models, materials, and lighting from images. In *CVPR*, pages 8280–8290, 2022. 3
- [41] Adam Paszke, Sam Gross, Soumith Chintala, Gregory Chanan, Edward Yang, Zachary DeVito, Zeming Lin, Alban Desmaison, Luca Antiga, and Adam Lerer. Automatic differentiation in pytorch. In *NIPS-W*, 2017. 6
- [42] Henry Peters, Yunhao Ba, and Achuta Kadambi. pcon: Polarimetric coordinate networks for neural scene representations. In *CVPR*, pages 16579–16589, 2023. 3
- [43] Matteo Poggi, Pierluigi Zama Ramirez, Fabio Tosi, Samuele Salti, Luigi Di Stefano, and Stefano Mattoccia. Cross-spectral neural radiance fields. In *3DV*, pages 606–616, 2022. 2
- [44] Yunshan Qi, Lin Zhu, Yu Zhang, and Jia Li. E2nerf: Event enhanced neural radiance fields from blurry images. In *ICCV*, pages 13254–13264, 2023. 2
- [45] Viktor Rudnev, Mohamed Elgharib, Christian Theobalt, and Vladislav Golyanik. Eventnerf: Neural radiance fields from a single colour event camera. In *CVPR*, pages 4992–5002, 2023. 2
- [46] Mingqi Shao, Chongkun Xia, Zhendong Yang, Junnan Huang, and Xueqian Wang. Transparent shape from a single view polarization image. In *ICCV*, pages 9277–9286, 2023. 3
- [47] Savvas Sfinaios, George Arvanitakis, Fotios K Konstantinidis, Georgios Tsimiklis, Angelos Amditis, and Panayiotis Frangos. A deep learning approach for pixel-level material classification via hyperspectral imaging. *arXiv preprint arXiv:2409.13498*, 2024. 7
- [48] Dor Verbin, Peter Hedman, Ben Mildenhall, Todd Zickler, Jonathan T Barron, and Pratul P Srinivasan. Ref-nerf: Structured view-dependent appearance for neural radiance fields. In *CVPR*, pages 5481–5490. IEEE, 2022. 3
- [49] Bruce Walter, Stephen R Marschner, Hongsong Li, and Kenneth E Torrance. Microfacet models for refraction through rough surfaces. In *Proceedings of the 18th Eurographics conference on Rendering Techniques*, pages 195–206, 2007. 4
- [50] Haoyuan Wang, Wenbo Hu, Lei Zhu, and Rynson WH Lau. Inverse rendering of glossy objects via the neural plenoptic function and radiance fields. In *CVPR*, pages 19999–20008, 2024. 3
- [51] Peng Wang, Lingjie Liu, Yuan Liu, Christian Theobalt, Taku Komura, and Wenping Wang. Neus: Learning neural implicit surfaces by volume rendering for multi-view reconstruction. *NeurIPS*, 34:27171–27183, 2021. 1, 3
- [52] Haoqian Wu, Zhipeng Hu, Lincheng Li, Yongqiang Zhang, Changjie Fan, and Xin Yu. Nefii: Inverse rendering for reflectance decomposition with near-field indirect illumination. In *CVPR*, pages 4295–4304, 2023. 3
- [53] Liwen Wu, Rui Zhu, Mustafa B Yaldiz, Yinhao Zhu, Hong Cai, Janarbek Matai, Fatih Porikli, Tzu-Mao Li, Manmohan Chandraker, and Ravi Ramamoorthi. Factorized inverse path tracing for efficient and accurate material-lighting estimation. In *ICCV*, pages 3848–3858, 2023. 3, 7
- [54] Yao Yao, Jingyang Zhang, Jingbo Liu, Yihang Qu, Tian Fang, David McKinnon, Yanghai Tsin, and Long Quan. Neif: Neural incident light field for physically-based material estimation. In *ECCV*, pages 700–716, 2022. 1, 3
- [55] Lior Yariv, Jiatao Gu, Yoni Kasten, and Yaron Lipman. Volume rendering of neural implicit surfaces. *NeurIPS*, 34:4805–4815, 2021. 2, 3, 5, 6, 7, 8
- [56] Lior Yariv, Peter Hedman, Christian Reiser, Dor Verbin, Pratul P Srinivasan, Richard Szeliski, Jonathan T Barron, and Ben Mildenhall. Bakedsd: Meshing neural sdf for real-time view synthesis. In *SIGGRAPH*, pages 1–9, 2023. 1
- [57] Lior Yariv, Yoni Kasten, Dror Moran, Meirav Galun, Matan Atzmon, Basri Ronen, and Yaron Lipman. Multiview neural surface reconstruction by disentangling geometry and appearance. *NeurIPS*, 33:2492–2502, 2020. 3
- [58] Tianxiang Ye, Qi Wu, Junyuan Deng, Guoqing Liu, Liu Liu, Songpengcheng Xia, Liang Pang, Wenxian Yu, and Ling Pei. Thermal-nerf: Neural radiance fields from an infrared camera. *arXiv preprint arXiv:2403.10340*, 2024. 2
- [59] Jingyang Zhang, Yao Yao, Shiwei Li, Jingbo Liu, Tian Fang, David McKinnon, Yanghai Tsin, and Long Quan. Neif++: Inter-reflectable light fields for geometry and material estimation. In *ICCV*, pages 3601–3610, 2023. 2, 3, 5

- [60] Kai Zhang, Fujun Luan, Qianqian Wang, Kavita Bala, and Noah Snavely. Physg: Inverse rendering with spherical gaussians for physics-based material editing and relighting. In *CVPR*, pages 5453–5462, 2021. 3
- [61] Xiuming Zhang, Pratul P Srinivasan, Boyang Deng, Paul Debevec, William T Freeman, and Jonathan T Barron. Nerfactor: Neural factorization of shape and reflectance under an unknown illumination. *ACM TOG*, 40(6):1–18, 2021. 3
- [62] Yuanqing Zhang, Jiaming Sun, Xingyi He, Huan Fu, Rongfei Jia, and Xiaowei Zhou. Modeling indirect illumination for inverse rendering. In *CVPR*, pages 18643–18652, 2022. 3
- [63] Jinyu Zhao, Yusuke Monno, and Masatoshi Okutomi. Polarimetric multi-view inverse rendering. *IEEE TPAMI*, 2022. 3